CORA Cork Open Research Archive
Cartlann Taighde Oscailte Chorcaí

Title	Continuously tunable Ku-band GaAs bandstop filter with reconfigurable all-pass capabilities
Authors	Fontana, Andrés;Psychogiou, Dimitra
Publication date	2025-06-26
Original Citation	Fontana, A. and Psychogiou, D. (2025) 'Continuously tunable Ku-band GaAs bandstop filter with reconfigurable all-pass capabilities', IEEE Microwave and Wireless Technology Letters, 35(9), pp. 1284-1287. https://doi.org/10.1109/LMWT.2025.3580893
Type of publication	Article (peer-reviewed);journal-article
Link to publisher's version	10.1109/lmwt.2025.3580893
Rights	© 2025, the Authors. This work is licensed under a Creative Commons Attribution 4.0 License. For more information, see https://creativecommons.org/licenses/by/4.0/ - https://creativecommons.org/licenses/by/4.0/
Download date	2026-11-15 13:59:33
Item downloaded from	https://hdl.handle.net/10468/18023



UCC
University College Cork, Ireland
Coláiste na hOllscoile Corcaigh

Continuously Tunable Ku-Band GaAs Bandstop Filter With Reconfigurable All-Pass Capabilities

Andrés Fontana, *Member, IEEE*, and Dimitra Psychogiou, *Senior Member, IEEE*

***Abstract*—A multiconfigurable monolithic microwave integrated circuit (MMIC) filter is reported. It exhibits three modes of operation, namely, a high-attenuation single-notch bandstop (BS) mode, a dual-notch BS mode, and an all-pass (AP) mode. It is based on a bridged-T network (BTN) using a minimum number of lumped elements and a signal cancellation technique to counteract the effect of the low on-chip quality factor. Transfer function tuning and bandstop-to-all-pass filter (BSF-to-AP) mode reconfigurability are readily obtained by tuning the frequency of two resonators. A prototype was manufactured using a pHEMT GaAs MMIC process exhibiting a BS mode with frequency tuning range (Δf_0) of 16% and suppression up to 68.5 dB, a dual-notch BS mode with Δf_0 of 15% and 20% fractional bandwidth (FBW), and an AP mode with insertion loss <5.3 dB.**

***Index Terms*—Bandstop filter (BSF), monolithic microwave integrated circuit (MMIC), multifunction device, tunable filter.**

I. Introduction

BANDSTOP filters (BSFs) are widely used to suppress the image frequency of radio frequency front ends (RFFEs) or to cancel interference or noise [1], [2]. Many tunable [3], [4], [5], [6], multiband [7], and multimode [8], [9], [10] BSFs have been reported utilizing high, moderate, and low unloaded quality factor (Q_u) technologies. High Q_u schemes using acoustic-wave resonators are limited to frequencies <2 GHz [11], [12], whereas waveguide-based components are very large in size [9], [13]. BSF demonstrations carried out on planar PCB [14], [15] and integrated circuit (IC) [16], [17], [18], [19], [20] technologies exhibit compact footprint and higher operational frequency but are limited by high loss. A continuously tunable SiGe BiCMOS BSF exhibiting rejection up to 70 dB but high-power consumption (70–90 mW) and complexity is reported in [2] employing active synthetic techniques. Other methods to counteract the low Q_u of microwave components in IC BSFs include signal canceling (SC) [13], [21], [22]. Passive distributed-element static BSFs with in-band rejection over 50 dB are reported in [21] using a two-path 180° out-of-phase cancellation implemented by PCB-based 3-dB 90° hybrid couplers and a bridged-T network (BTN) without frequency tunability or multifunctional operation. The hybrid couplers method was also applied to X-band GaAs monolithic microwave IC (MMIC) tunable BSFs [22] and to PCB-based SIW coaxial cavity bandstop-to-all-pass filters (BSF-to-AP) at S-band [13]. Whereas the approach in [22] requires several lumped elements and does not possess multifunctional capabilities, the reconfigurable BSF-to-AP concept in [13] exhibits large footprint.

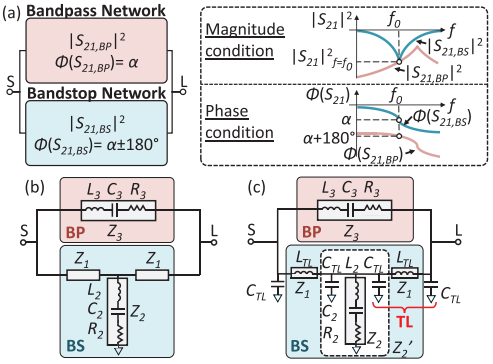


Fig. 1. (a) High-suppression BSF employing a two-path out-of-phase SC. (b) BTN implementation with generic Z_1 impedance. (c) Modification with π-type TL.

This work demonstrates the potential to realize GaAs-based MMIC BSFs at Ku-band with high attenuation, tunable center frequency (f_0), and a reconfigurable BSF-to-AP operation. The proposed concept is based on a BTN approach with minimum number of components using self-interference cancellation to mitigate the low Q_u of on-chip varactors. Continuously tunable deep-rejection operation is enabled to effectively manage interference of closely spaced channels in the upcoming frequency range 3 (FR3) band (~6–22 GHz), critical for civil applications, satellite communications, automotive and military radar systems, and among others. A comprehensive design methodology is presented taking into consideration the capabilities of a commercially available GaAs process.

II. Theoretical Foundations

The BSF-to-AP concept based on a BTN is illustrated in Fig. 1. Whereas Naglich et al. [13] also showed BSF-to-AP functionality, it employs a different topology analyzed by coupled-resonator-based synthesis. To implement the two-path 180° out-of-phase SC, the input signal is divided between a bandpass (BP)-type and a bandstop (BS)-type network [Fig. 1(a)]. Their forward transmission magnitude ($|S_{21,BP}|$ and $|S_{21,BS}|$) and phase [$\phi(S_{21,BP})$ and $\phi(S_{21,BS})$] must satisfy (1) and (2) at f_0 [21]

$$\left|S_{21,BP}\right|^2_{f=f0} = \left|S_{21,BS}\right|^2_{f=f0} \tag{1}$$

$$\phi(S_{21,BP})\big|_{f=f0} + \phi(S_{21,BS})\big|_{f=f0} = \pm 180°. \tag{2}$$

Received 16 April 2025; accepted 28 May 2025. Date of publication 26 June 2025; date of current version 17 September 2025. This work was supported by the Research Ireland (RI) under Grant 20/RP/8334. *(Corresponding author: Andrés Fontana.)*

Andrés Fontana is with the Tyndall National Institute, Cork, T12 R5CP Ireland (e-mail: afontana@ieee.org).

Dimitra Psychogiou is with the School of Engineering, University College Cork, Cork, T12 K8AF Ireland, and also with the Tyndall National Institute, Cork, T12 R5CP Ireland (e-mail: dpsychogiou@ucc.ie).

Digital Object Identifier 10.1109/LMWT.2025.3580893

© 2025 The Authors. This work is licensed under a Creative Commons Attribution 4.0 License.
For more information, see https://creativecommons.org/licenses/by/4.0/

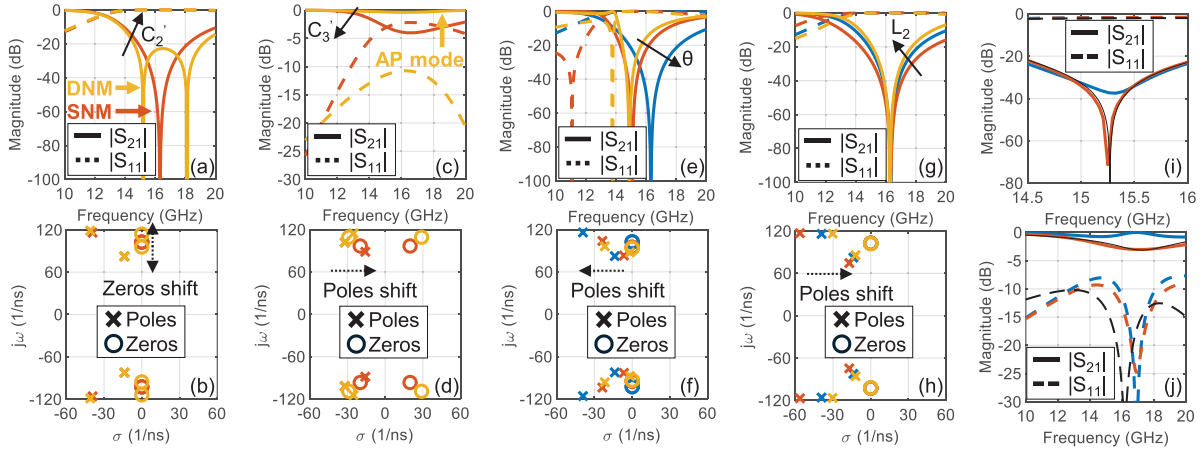


Fig. 2. (a) BSF mode S-parameters and (b) pole-zero plot for $L_2 = L_3 = 0.563$ nH, $C_3 = 120$ fF, $R_2 = R_3 = 0\ \Omega$, $Z_{0TL} = 50\ \Omega$, and $\theta = 45°$: SNM ($C_2' = 86.24$ fF) and DNM ($C_2' = 80$ fF). (c) AP mode S-parameters and (d) pole-zero plot for $L_2 = L_3 = 0.563$ nH, $C_2 = 120$ fF, $R_2 = R_3 = 0\ \Omega$, $Z_{0TL} = 50\ \Omega$, $\theta = 45°$, and $C_3' = 66, 105$ fF. (e) SNM BSF mode S-parameters and (f) pole-zero plot for $L_2 = L_3 = 0.563$ nH, $R_2 = R_3 = 0\ \Omega$, $Z_{0TL} = 50\ \Omega$, and θ variations: 10° ($C_3 = 175$ fF and $C_2' = 174.26$ fF), 25° ($C_3 = 147$ fF and $C_2' = 139.07$ fF), and 45°($C_3 = 120$ fF and $C_2' = 86.24$ fF). (g) SNM BSF mode S-parameters and (h) pole-zero plot for $R_2 = R_3 = 0\ \Omega$, $Z_{0TL} = 50\ \Omega$, and $\theta = 45°$ for: $L_2 = L_3 = 0.2$ nH ($C_3 = 190$ fF and $C_2' = 100.95$ fF), $L_2 = L_3 = 0.563$ nH ($C_3 = 120$ fF and $C_2' = 86.24$ fF), and $L_2 = L_3 = 0.8$ nH ($C_3 = 95$ fF and $C_2' = 73.92$ fF). BSF-to-AP S-parameters for $L_2 = L_3 = 0.563$ nH, $R_2 = R_3 = 4\ \Omega$, $Z_{0TL} = 50\ \Omega$, and $\theta = 25°$ for (i) SNM ($C_2' = 139.07$ fF) with $C_3 = 147$ fF (blue trace) and $C_3' = 145.63$ fF (orange trace) and (j) AP mode ($C_2 = 147$ fF) for $C_3' = 93$ fF ($R_2 = R_3 = 0\ \Omega$, blue trace) and $C_3' = 93$ fF ($R_2 = R_3 = 4\ \Omega$, orange trace). Black traces: circuit simulations.

The generic block diagram in Fig. 1(a) can be represented by a BTN [21], [23] [Fig. 1(b)], where Z_2 and Z_3 are impedances that can be implemented by series lossy resonators (L_2, C_2, and R_2 and L_3, C_3, and R_3). The magnitude condition in (1) can be obtained by either setting the resonators at the same [23] or different frequencies, and the impedance Z_1 can be used to introduce an extra phase delay to satisfy (2) [see Fig. 1(a)]. In [23], the synchronous resonators with lumped resistors were used to meet (1), while (2) was met by replacing Z_1 by a series capacitor. In this work, asyncronous resonator tuning is being used, while the phase delay in (2) is implemented by a transmission line (TL) with characteristic impedance Z_{0TL}, electrical length $\theta < 90°$, and it is modeled by its π-type first-order low-pass equivalent [C_{TL} and L_{TL} in Fig. 1(c)]. RF tuning is incorporated without lumped resistors by means of embedded varactors that facilitate the realization of three distinct modes of operation, namely, a single-notch mode (SNM), a dual-notch mode (DNM), and an all-pass (AP) mode.

A. Lossless BTN BSF-to-AP

The BTN analysis starts by considering $R_2 = R_3 = 0\ \Omega$ and neglecting C_{TL} at the input/output. To enable the S-parameters calculation from the impedance matrix of the BTN [23], C_{TL} is regrouped with Z_2, forming a series impedance Z_2', while L_{TL} describes Z_1'. Then, Z_1, Z_2', and Z_3 can be calculated using the following:

$$Z_1(\omega) = jZ_{0TL}\sin(\theta) \tag{3}$$

$$Z_2'(\omega) = -j\frac{L_2C_2\omega^2 - 1}{(2L_2C_{TL}\omega^3 - \omega)C_2 - 2C_{TL}\omega} \tag{4}$$

$$Z_3(\omega) = -j(2C_3L_3\omega + 1)C_3^{-1}\omega^{-1}. \tag{5}$$

Using conventional Z-to-S-parameter conversion, the S-parameters and pole-zero diagrams of the BSF-to-AP are computed and provided in Fig. 2 for a BSF implementation considering realistic GaAs MMIC component values (L_2, $L_3 \approx 0.15$–1.5 nH and C_2, $C_3 \approx 0.05$–1.2 pF). Specifically, Fig. 2(a) illustrates how the BS attenuation evolves as a function of C_2 ($\theta = 45°$) for an SNM with deep attenuation at $f \approx f_0 = 16$ GHz when detuning the BS ($C_2' = C_2 + \Delta C_2$) from the BP resonating at 15 GHz, and a DNM with smaller C_2' value than in SNM, achieving lower attenuation and equi-ripple response. Fig. 2(b) depicts the pairs of dominating complex conjugate poles and zeros for the SNM and DNM cases in Fig. 2(a). When detuning C_2', the zeros are displaced, while the complex conjugate poles remain almost unaffected. Fig. 2(c) exhibits the AP mode obtained when detuning the BP ($C_3' = C_3 + \Delta C_3$) from the BS resonating at f_0. Fig. 2(d) displays a symmetrical configuration of complex conjugate zeros and their displacement along the s plane until achieving an AP response (yellow trace). If θ is shortened to reduce the device footprint, C_2', C_3, and $L_2 = L_3$ must be recalculated to maintain the SC. Fig. 2(e) shows three SNM examples for $\theta = 45°$, 25°, and 10°. As θ is reduced, the poles get closer to the axis $j\omega$ [Fig. 2(f)] and approach f_0, causing a steeper roll-off. Fig. 2(g) and (h) depicts how L_2 and L_3 affect the transfer function for a given θ, resulting in a more selective notch for larger inductors owing to the poles shift toward the axis $j\omega$ [Fig. 2(h)].

B. Lossy BSF-to-AP

In the case of lossy resonators ($R_2 = R_3 > 0\ \Omega$), the BTN impedances are rewritten as $Z_{3Lossy} = R_3 + Z_3$ and $Z_{2Lossy}' = (C_2^2R_2)/A + jB/(A\omega)$, with A and B defined in (6) and (7), as shown at the bottom of the next page. As shown in Fig. 2(i), the effect of loss can be counteracted by slightly optimizing the device with a circuit simulator. This approach enables the use of lossy GaAs MMIC on-chip varactors, typically $Q_u \geq 15$ ($R \leq 4\ \Omega$), by exploiting destructive signal interference. However, as the varactor losses increase, a degradation in the AP mode around f_0 is observed. Fig. 2(j) depicts a comparison between the lossless and the lossy AP modes using the worst varactor condition ($Q_u = 15$ or $R = 4\ \Omega$).

Finally, a comparison of the corrected transfer functions calculated in MATLAB and using circuit simulations in Keysight ADS is depicted in Fig. 2(i) and (j). A good agreement

TABLE I
COMPARISON WITH THE STATE-OF-THE-ART BSFS

MMIC tech.	Multiband/Multimode	Δf_0 (GHz), [TR]	Stopband max. rejection (dB)	RL@f_0	IL@$_{6\,GHz}$ (dB)	Size (λg^2, mm^2)	Ref.
GaAs	**No/BSF-to-AP**	**14.76-17.17, [1.16:1]**	**68.5**	**2.8**	**0.70**	**0.0351,1.026**	**T.W.**
	No/No	8.7-10.5, [1.21:1]	73.6	N.A	2.30	0.0014, 1.566	[22]
	No/No	7.2$^{\#}$, N.A	23.7	17.3	1.10	0.0006, 1.178	[20]
	Dual-Band/No	4.8/9.6$^{\#}$, N.A	16.6/17.8	15.9/10.1	0.73	0.0002, 4.000	[18]
CMOS	No/No	53.2$^{\#}$, N.A	14.2	1.8	N.A.	0.0017, N.A	[16]
	No/No	19.0$^{\#}$, N.A	37.0	N.A	0.60	N.A, 0.028	[24]
	No/No	27.4-31.6, [1.15:1]	35.0	N.A	2.70/3.50	N.A, 0.036	[19]
SiGe BiCMOS	No/No	8.0-16.0, [2:1]	70.0	N.A	N.A.	N.A, 0.350	[2]

T.W.: This work (Values informed for SNM), $^{\#}$Static device, N.A: Not available, TR: Tuning range.

is obtained, successfully validating the proposed modeling technique. Small discrepancies are due to the omission of C_{TL} in the mathematical model. Based on these observations, the following design steps can be used as a guideline. First, design BP and BS resonators to resonate at $f_{0\,max}$ for example with $L_2 = L_3$ and $C_2 = C_3$, ensuring the relationship among L_2 and C_2 and L_3 and C_3 [Fig. 2(g)], and θ [Fig. 2(e)] meets the fractional bandwidth (FBW) specifications. Then, slightly reduce C_2 to detune the BS resonator and satisfy (1) and (2). Next, estimate varactor tuning ranges $\Delta C_2 = C_{2\,max} - C_{2\,min}$ and $\Delta C_3 = C_{3\,max} - C_{3\,min}$ at $f_{0\,min}$, keeping L_2 or L_3 fixed. A larger Δf_0 increases tuning range and losses R_2 and R_3, which affects IL in the AP mode. Estimate IL_{max} with $C_2 = C_{2\,max}$ and $C_3 = C_{3\,min}$. If the specifications are not met, a tradeoff between Δf_0 (SNM and DNM) and IL (AP mode) should be established.

III. EXPERIMENTAL VALIDATION

A photograph of the manufactured BSF-to-AP prototype based on the circuit schematic in Fig. 1(c) and using a WIN Semiconductor PQH1-0P 0.18-μm InGaAs pHEMT process is depicted in Fig. 3(a). L_2 and L_3 were implemented with their microstrip distributed equivalent to minimize the number of lumped components. C_2 and C_3 were implemented by two-finger E-gate transistors with gate widths 40 and 38 μm [22], leading to a measured C_2 = 51–256 fF, C_3 = 75–267 fF, and $Q_{u\,min} \approx 15$. Fig. 3(b) shows the measured S-parameters covering the FR3 spectrum expected to be allocated for 6G wireless services, when configured in the SNM and tuned from 14.8 to 17.2 GHz ($\Delta f_0 \approx 16\%$). It exhibits an in-band return loss (RL) $\leq$ 2.8 dB, a −20-dB FBW of 15.8%–15%, and a max./min. suppression of 68.5/50.8 dB (63.1 dB avg. from 20 samples). When tuned in the DNM, the filter can achieve a broader −20-dB FBW in expense of maximum 20-dB suppression [Fig. 3(c)], obtaining Δf_0 = 15.2%, FBW between 20.2% and 21.5%, and in-band RL $\leq$ 2.6 dB. In the AP mode [Fig. 3(d)], the filter is tuned to provide the minimum IL possible and RL better than 10 dB. Measurements show a min./max. IL of 0.7/5.3 dB at 6/15.72 GHz. Table I compares this work with the state-of-the-art MMIC BSFs. The BSF-to-AP concept introduces a simple design with minimum number

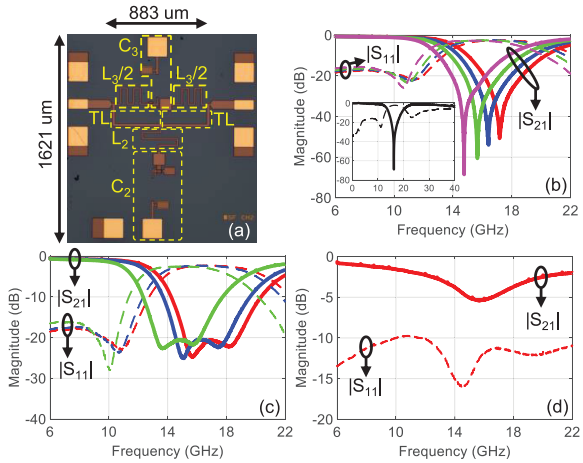


Fig. 3. BSF-to-AP. (a) Manufactured prototype with: L_2 = 0.536 nH, C_2 = 51–256 fF, R_2 = 4.83 Ω, L_3 = 1.072 nH, C_3 = 75–267 pF, R_3 = 4.56 Ω, Z_{0TL} = 73 Ω, θ = 25°, C_{TL} = 47.05 fF, and L_{TL} = 0.224 nH. Measured S-parameters. (b) SNM. (c) DNM. (d) AP mode.

of elements that enables the realization of reconfigurable multimode operation with only two tunable varactors. In its SNM, the device shows a better tuning range than in [19] and deep notch suppression comparable to the best MMIC BSFs reported in [2] and [22].

IV. CONCLUSION

This work advances tunable, multifunctional devices for modern wireless RFFEs by tackling the challenges of low Q_u on-chip varactors to implement deep-notch BSFs. The BTN enables SC, BW tuning (DNM), and BSF switch-off operation (AP mode) without extra components. To the best of our knowledge, such features have not been reported in MMICs. The manufactured prototype shows a multiconfigurable GaAs MMIC BSF-to-AP with: 1) a BS mode with Δf_0 of 16% and 68.5-dB suppression; 2) a dual-notch BS mode with Δf_0 of 15.2% and FBW = 20.2%; and 3) an AP mode with IL <5.3 dB.

ACKNOWLEDGMENT

The authors would like to acknowledge WIN Semiconductors for providing the manufactured samples.

$$A = 4C_2^2C_{TL}^2L_2\omega^4 + 4C_2^2\left(C_{TL}^2R_2^2 - L_2C_{TL}\right)\omega^2 + \left(C_2^2 - 8C_2C_{TL}^2L_2 + 4C_2C_{TL} + 4C_{TL}^2\right) \quad (6)$$

$$B = -2C_{TL}C_2^2L_2^2\omega^4 + \left(C_2^2L_2^2 - 2C_{TL}C_2^2R_2^2 + 4C_{TL}C_2L_2\right)\omega^2 - C_2 - 2C_{TL} \quad (7)$$

REFERENCES

[1] Y.-C. Ou and G. M. Rebeiz, "Lumped-element fully tunable bandstop filters for cognitive radio applications," *IEEE Trans. Microw. Theory Techn.*, vol. 59, no. 10, pp. 2461–2468, Oct. 2011, doi: 10.1109/TMTT.2011.2160965.

[2] L. Mohammadi and K.-J. Koh, "Integrated synthetic bandstop filters for blocker rejection at RF and microwave frequency bands," *IEEE Trans. Microw. Theory Techn.*, vol. 64, no. 11, pp. 3557–3567, Nov. 2016, doi: 10.1109/TMTT.2016.2602867.

[3] Y. Feng, S. Tiwari, S. A. Bhave, and R. Wang, "Micromachined tunable magnetostatic forward volume wave bandstop filter," *IEEE Microw. Wireless Technol. Lett.*, vol. 33, no. 6, pp. 807–810, Jun. 2023, doi: 10.1109/LMWT.2023.3267449.

[4] Y.-H. Cho, C. Park, and S.-W. Yun, "4-pole tunable absorptive bandstop filters using folded coupled-lines with an inductor," *IEEE Access*, vol. 10, pp. 120191–120199, 2022, doi: 10.1109/ACCESS.2022.3221461.

[5] P. Adhikari, W. Yang, Y.-C. Wu, and D. Peroulis, "A PCB technology-based 22–42-GHz quasi-absorptive bandstop filter," *IEEE Microw. Wireless Compon. Lett.*, vol. 28, no. 11, pp. 975–977, Nov. 2018, doi: 10.1109/LMWC.2018.2867108.

[6] S. Saeedi, J. Lee, and H. H. Sigmarsson, "Novel coupling matrix synthesis for single-layer substrate-integrated evanescent-mode cavity tunable bandstop filter design," *IEEE Trans. Microw. Theory Techn.*, vol. 63, no. 12, pp. 3929–3938, Dec. 2015, doi: 10.1109/TMTT.2015.2490075.

[7] D. Li and K. Xu, "Multifunctional switchable filter using coupled-line structure," *IEEE Microw. Wireless Compon. Lett.*, vol. 31, no. 5, pp. 457–460, May 2021, doi: 10.1109/LMWC.2021.3067893.

[8] J. Lee, E. J. Naglich, H. H. Sigmarsson, D. Peroulis, and W. J. Chappell, "New bandstop filter circuit topology and its application to design of a bandstop-to-bandpass switchable filter," *IEEE Trans. Microw. Theory Techn.*, vol. 61, no. 3, pp. 1114–1123, Mar. 2013, doi: 10.1109/TMTT.2012.2237036.

[9] T. Yang and G. M. Rebeiz, "Bandpass-to-bandstop reconfigurable tunable filters with frequency and bandwidth controls," *IEEE Trans. Microw. Theory Techn.*, vol. 65, no. 7, pp. 2288–2297, Jul. 2017, doi: 10.1109/TMTT.2017.2679182.

[10] D. Psychogiou, "Reconfigurable all-pass-to-bandstop acoustic-wave-lumped-element resonator filters," *IEEE Microw. Wireless Compon. Lett.*, vol. 30, no. 8, pp. 745–748, Aug. 2020, doi: 10.1109/LMWC.2020.3004028.

[11] D. Psychogiou, R. Gómez-García, and D. Peroulis, "High- Q bandstop filters exploiting acoustic-wave-lumped-element resonators (AWLRs)," *IEEE Trans. Circuits Syst. II, Exp. Briefs*, vol. 63, no. 1, pp. 79–83, Jan. 2016, doi: 10.1109/TCSII.2015.2505078.

[12] N. S. Luhrs, D. J. Simpson, and D. Psychogiou, "Multiband acoustic-wave-lumped-element resonator-based bandpass-to-bandstop filters," *IEEE Microw. Wireless Compon. Lett.*, vol. 29, no. 4, pp. 261–263, Apr. 2019, doi: 10.1109/LMWC.2019.2901199.

[13] E. J. Naglich, J. Lee, D. Peroulis, and W. J. Chappell, "Switchless tunable bandstop-to-all-pass reconfigurable filter," *IEEE Trans. Microw. Theory Techn.*, vol. 60, no. 5, pp. 1258–1265, May 2012, doi: 10.1109/TMTT.2012.2188723.

[14] C. Karpuz, A. K. Gorur, and M. Emur, "Quad-band microstrip bandstop filter design using dual-mode open loop resonators having thin film capacitors," *IEEE Microw. Wireless Compon. Lett.*, vol. 26, no. 11, pp. 873–875, Nov. 2016, doi: 10.1109/LMWC.2016.2615092.

[15] N. Jankovic, R. Geschke, and V. Crnojevic-Bengin, "Compact tri-band bandpass and bandstop filters based on Hilbert-fork resonators," *IEEE Microw. Wireless Compon. Lett.*, vol. 23, no. 6, pp. 282–284, Jun. 2013, doi: 10.1109/LMWC.2013.2258005.

[16] S. K. Thapa, R. K. Pokharel, B. Chen, and A. Barakat, "On-chip millimeter-wave DGS based bandstop filter in 0.18-μm CMOS process," *IEEE Trans. Circuits Syst. II, Exp. Briefs*, vol. 69, no. 6, pp. 2732–2736, Jun. 2022, doi: 10.1109/TCSII.2022.3158995.

[17] V. N. R. Vanukuru and V. K. Velidi, "Millimeter-wave CMOS 30/80 GHz sharp-rejection dual-band bandstop filters using TFMS open-stepped-impedance resonators," *IEEE Trans. Circuits Syst. II, Exp. Briefs*, vol. 68, no. 1, pp. 201–205, Jan. 2021, doi: 10.1109/TCSII.2020.3006198.

[18] Y.-S. Lin, Y.-C. Huang, and Q.-Y. Jiang, "Miniature dual-band absorptive bandstop filters with improved passband performance," *IEEE Trans. Circuits Syst. I, Reg. Papers*, vol. 69, no. 6, pp. 2339–2350, Jun. 2022, doi: 10.1109/TCSI.2022.3155491.

[19] T. Zhang, J. Pan, B. Liu, H. Zhang, and Z. Zhu, "Miniaturized wideband pole-zero following tunable bandstop filter for 5G millimeter-wave application," *IEEE Trans. Circuits Syst. II, Exp. Briefs*, vol. 71, no. 8, pp. 3725–3729, Aug. 2024, doi: 10.1109/TCSII.2024.3368001.

[20] E.-W. Chang and Y.-S. Lin, "Miniature multi-band absorptive bandstop filter designs using bridged-T coils," *IEEE Access*, vol. 6, pp. 73637–73646, 2018, doi: 10.1109/ACCESS.2018.2882828.

[21] D. R. Jachowski, "Passive enhancement of resonator Q in microwave notch filters," in *IEEE MTT-S Int. Microw. Symp. Dig.*, vol. 3, Fort Worth, TX, USA, Jun. 2004, pp. 1315–1318, doi: 10.1109/MWSYM.2004.1338808.

[22] K. Zhao and D. Psychogiou, "X-band MMIC-based tunable quasi-absorptive bandstop filter," *IEEE Microw. Wireless Technol. Lett.*, vol. 33, no. 4, pp. 391–394, Apr. 2023, doi: 10.1109/LMWT.2022.3228572.

[23] J. S. Chieh and J. Rowland, "Quasi-lumped element bridged-T absorptive bandstop filter," *IEEE Microw. Wireless Compon. Lett.*, vol. 26, no. 4, pp. 264–266, Apr. 2016, doi: 10.1109/LMWC.2016.2537787.

[24] L. Chen, H. Zhu, R. Gómez-García, and X. Zhu, "Miniaturized on-chip notch filter with sharp selectivity and >35-dB attenuation in 0.13-μm bulk CMOS technology," *IEEE Electron Device Lett.*, vol. 43, no. 8, pp. 1175–1178, Aug. 2022, doi: 10.1109/LED.2022.3184920.